2

Chemical processes for the synthesis of nanostructured materials

M. Gusatti[1], D. A. R. Souza[1], M. Durazzo[2] and H. G. Riella[1]

[1]Materials and Corrosion Laboratory (LABMAC), Chemical Engineering Department, Federal University of Santa Catarina, P.O. 476, Trindade, 88040-900, Florianópolis, SC, Brazil
[2]Nuclear Energy Research Institute (IPEN), Avenida Lineu Prestes 2242, Cidade Universitária, 05508-000, São Paulo, SP, Brazil

Outline:

Introduction

The fascinating and uncommon properties of nanomaterials have attracted considerable interest among scientists to explore their uses in various technological fields. Nanoparticles are a part of nanomaterials where at least one characteristic dimension is less than 100 nm. At this scale, the nanomaterials show new and interesting properties not seen in their conventional bulk counterparts. These emergent properties of nanomaterials are mainly due to increased relative surface area and quantum effects [1].

Semiconducting metal oxides are the most versatile nanomaterials because of their various properties and functionalities in many areas of chemistry, physics, and materials science. In particular, zinc oxide (ZnO) is an attractive *n*-type semiconductor with a wide band gap (3.37 eV) and a large exciton binding energy of 60 meV at room temperature [2-3]. The exciton binding energy of ZnO is much higher than those of other interesting materials such as ZnSe, ZnS, and GaN, which makes it an excellent semiconductor for lasing [4]. This material has been important in fundamental studies, and it possesses unique optical, electronic, and mechanical properties [5-8]. ZnO exhibits the most diverse and abundant configurations of nanostructures known to date, such as nanorods, nanobelts, nanohelixes, nanorings, nanowires, nanoneedle, nanowalls, and nanoflowers [9-13]. Zinc oxide is a multifunctional material that plays an essential role in the manufacturing of catalysts, sensors, piezoelectric transducers, paints, ceramics, varistors, cosmetics and transparent UV protective films [14-17]. Therefore, much effort has been devoted towards the synthesis of ZnO.

Titanium dioxide (TiO_2) is a metal oxide that has been widely investigated due to their unique properties and various industrial applications in photocatalysis, solar cells, pigments, photovoltaic devices, sensors, electrochromic devices, and cosmetics [18-26]. TiO_2 occurs naturally in three different forms which are, in order of abundance, rutile, anatase, and brookite. The rutile and anatase phases have been intensively researched and display significant technological uses, mainly due to their optical properties [27]. The anatase form shows a better photo catalytic activity and antibacterial performance [28-29]. TiO_2 nanoparticles have been widely used as an efficient catalyst for the decomposition of organic contaminants present in water [30-31]. Titanium dioxide has other remarkable properties such as redox selectivity, high chemical and thermal stability, high photoactivity and wide band gap (3.2 eV for anatase phase) [32-37]. The various important applications of TiO_2 nanoparticles can also be attributed to the easiness of its synthesis, its low cost and low toxicity [38].

Rare earth oxides have been extensively investigated due to their fascinating electronic, optical, and chemical properties resulting from their 4f electrons [39-40]. These properties depend strongly on the material's chemical composition, crystal structure, shape, and dimensionality [40]. Among rare earth oxides, gadolinium oxide (Gd_2O_3) is an attractive material due to its vast area of applications. It has interesting properties such as good chemical durability, thermal and photochemical stabilities, and low phonon energy [41-42]. Gadolinium oxide is a promising candidate for different applications because of its high refractive index, wide band gap (5.4 eV), low phonon energy, suitable permittivity, and its ability of being easily doped with rare earth ions [43-45]. This material has been proposed in optoelectronic devices, data storage, sensors, semiconductor devices, and display technologies [46-47]. Recently Gd_2O_3 nanoparticles have been attracting scientific attention because of their capacity to improve imaging techniques such as magnetic resonance imaging (MRI) [48-49].

Owing to promising applications and excellent properties, a wide range of studies on new synthetic routes to prepare ZnO, TiO_2 and Gd_2O_3 nanomaterials have been performed over the years. Many

different methods, including microwave-assisted synthesis, hydrothermal processing, co-precipitation method, mechanochemical processing, sol-gel technique, spray pyrolysis and solochemical processing [50-54], have been devised to prepare ZnO nanostructures. Among these methods, the solochemical processing is of particular interest because of its reproducibility, simplicity, and reliability [54]. Moreover, this technique provides a promising alternative for low cost and large-scale production of ZnO nanostructures [53]. The solochemical processing consists basically in the reaction between a heated alkaline solution and another containing the precursor (zinc complex) at room temperature [53-55]. In this approach, the synthesis of the ZnO nanostructures is performed using mild reaction conditions, simple procedure and equipment, and short reaction time.

Preparation of nanosized TiO_2 has been carried out by methods such as solvothermal technique, microwave method, hydrothermal process and sol-gel synthesis [56-59]. Among these approaches, sol–gel syntheses from titanium alkoxides are the most widely used. The production of metal oxides by this method generally involves hydrolysis and condensation reactions of titanium alkoxide dissolved in an organic solvent with controlled amounts of water [60-61]. Complete reactions and loss of solvent leads to the transition from the liquid sol into a solid gel phase [61]. The sol-gel process offers several advantages such as low reaction temperature, better homogeneity, high purity, and low cost [62]. In this method, it is possible to control the size and morphology of the particle by regulating the sol composition, reaction temperature, nature of solvent, calcination temperature, and reaction time. In addition, a prolonged heating time at low temperature for the gel can avoid the agglomeration of the TiO_2 nanoparticles during the crystallization process [63].

Efforts have also been made to develop different methods for preparing gadolinium oxide nanostructures. They include: magnetron sputtering, precipitation technique, solvothermal synthesis and polyol method [44, 64-66]. The polyol method is a promising technique for the synthesis of nanoparticles and has been successfully used to obtain a large variety of materials, including oxides. It is based on the direct precipitation of oxides in a high boiling point alcohol [67-68]. Since the alcohol acts as a surface capping agent, the polyol route allows a close control of the particle size [69]. Some experimental conditions such as temperature and precursor concentration can also be adjusted to prepare nanomaterials with controlled size and shape [69]. Besides, the polyol process stands out as an efficient route to produce monodisperse and non-agglomerated nanoparticles compared to other synthetic routes [68].

This chapter describes the solochemical, polyol and sol-gel routes for the production of ZnO, Gd_2O_3, and TiO_2 nanostructures, respectively. The effects of the reaction conditions on the formation of the ZnO nanocrystals, the influence of calcination temperature on the size and shape of the Gd_2O_3 nanoparticles, and the effect of heat treatment time on the preparation of TiO_2 nanostructures will be discussed.

Solochemical Technique

Rapid development in the applications of the nanomaterials, ranging from electro-optics to biology, demands precise control of their size, shape and properties [70-71]. Several physical and chemical routes have been introduced to prepare nanostructures with various sizes and morphologies. Synthesis of nanostructures via physical methods generally involves complex procedures, sophisticated equipment, and relatively high pressure and temperature. In contrast, chemical methods comprise a simple and versatile option for the preparation of nanostructures due to lower

synthesis temperature and higher product uniformity [72-73]. Some of these chemical methods require a relatively high growth temperature (above 100 °C), long reaction durations, high pressures, and several processing steps. Other chemical approaches require surfactants and additives for tailoring the shape and size of nanostructures, which can introduce impurities into the desired products. Such disadvantages make some chemical techniques unfavorable for the production of nanomaterials.

The solochemical method stands out as an efficient chemical route for preparing nanomaterials or nano-composites with high purity. This method comprises the preparation of a solution containing the precursor, and the subsequent decomposition of said precursor at a suitable temperature into the desired nanostructures, with no additional processing requirements [53-54, 74]. This route involves a minimum number of steps and reactants, which avoids undesirable excess of starting materials, parallel reactions, and byproducts that can contaminate the final product. The solochemical process is successfully used to prepare ZnO nanostructures [53-55], and can also be applied to different precursors to form other nanostructured oxides such as Mn_2O_3 and NiO [53], and nanocomposites like ZnO/TiO_2 [75].

The solochemical synthesis of ZnO nanostructures consists of chemical reactions between a heated alkaline solution, such as NH_4OH [53] or NaOH [54-55], and a zinc precursor solution under controlled temperature and slow reagent mixture. In this process, the reactions take place at relatively low temperatures (below 100 °C) using a short reaction time [76]. Furthermore, the solochemical processing has other advantages such as easy procedure, simple equipment, low-cost, and the products do not require subsequent thermal treatment after the drying step. In this method, by controlling the growth parameters like pH value [77] and reaction temperatures [55, 76], rounded nanoparticles and rod-like structures can be achieved, and the size and optical properties of the ZnO nanostructures can also be tuned. No templates, surface capping agents, catalysts, or other additives are necessary to produce the ZnO nanostructures through this technique [78]. Thus, this processing may be one of the simplest and appropriate chemical routes to meet the industrial needs of ZnO nanocrystals.

The formation mechanism of the ZnO nanostructures is a complex process and mostly considered to include two main steps: the generation of a ZnO nuclei, and subsequent ZnO crystal growth. In a typical aqueous solution approach, the $Zn(OH)_4^{2-}$ complexes serve as basic growth units for the preparation of ZnO nanostructures [79-81]. Therefore, in the solochemical reaction the Zn^{2+} ions are produced from the zinc precursor and react with the OH^- ions to produce $Zn(OH)_4^{2-}$ complexes [76, 78]. When their concentration reaches the degree of supersaturation, a part of these growth units decompose to form ZnO nuclei, and the nucleation process is initiated. At last, the growth of the nuclei took place along the polar *c*-axis of the ZnO structure by means of the incorporation of growth units on the growth interfaces (0001), resulting in ZnO nanostructures [78].

In a typical solochemical synthesis, the precursor solution was prepared by dissolving an appropriate amount of zinc precursor in deionized water. The concentration of zinc precursor solution was kept below 0.6 M. The alkaline solution was obtained by dissolving a given quantity of sodium hydroxide (NaOH) in deionized water. This solution was then heated to a certain temperature ranging from 50 °C to 90 °C in a reactor until a clear solution was formed. Following, the zinc precursor solution was slowly injected into the hot alkaline solution under vigorous stirring. During this step, the injection of zinc solution does not considerably change the temperature of the reaction mixture. After injection, the previously transparent mixture acquires white coloring indicating the formation of ZnO nanocrystals. The heating and stirring of the mixture usually continue for 2 h, and the refluxing temperature is maintained at the same value chosen at the beginning of the reaction. Then, the product is filtered and washed with deionized water and dried

at low temperature for several hours. In order to systematically study the parameters affecting the solochemical synthesis of ZnO nanocrystals, different temperatures, kinds of zinc sources, duration of reaction, and concentration of the zinc precursor solution were investigated.

Figure 2.1 shows the XRD patterns of the samples obtained by the solochemical reaction between sodium hydroxide and zinc chloride ($ZnCl_2$) (Fig. 2.1(a)) or zinc nitrate hexahydrate ($Zn(NO_3)_2 \cdot 6H_2O$) (Fig. 2.1(b)) under the same experimental conditions. The reactions with both zinc precursors were performed at different temperatures (50 °C, 70 °C and 90 °C). All XRD patterns are similar and can be explained only by the hexagonal wurtzite structure (space group $P6_3mc$) of ZnO, reported in ICSD [82] card No. 57 450. These results indicate that even the samples synthesized at lower reaction temperature have a well-defined crystalline structure. The diffraction peaks of the ZnO samples obtained with both precursors at all reaction temperatures are considerably more broadened than those presented by bulk sample, which is a particular feature of nanometer-scale materials.
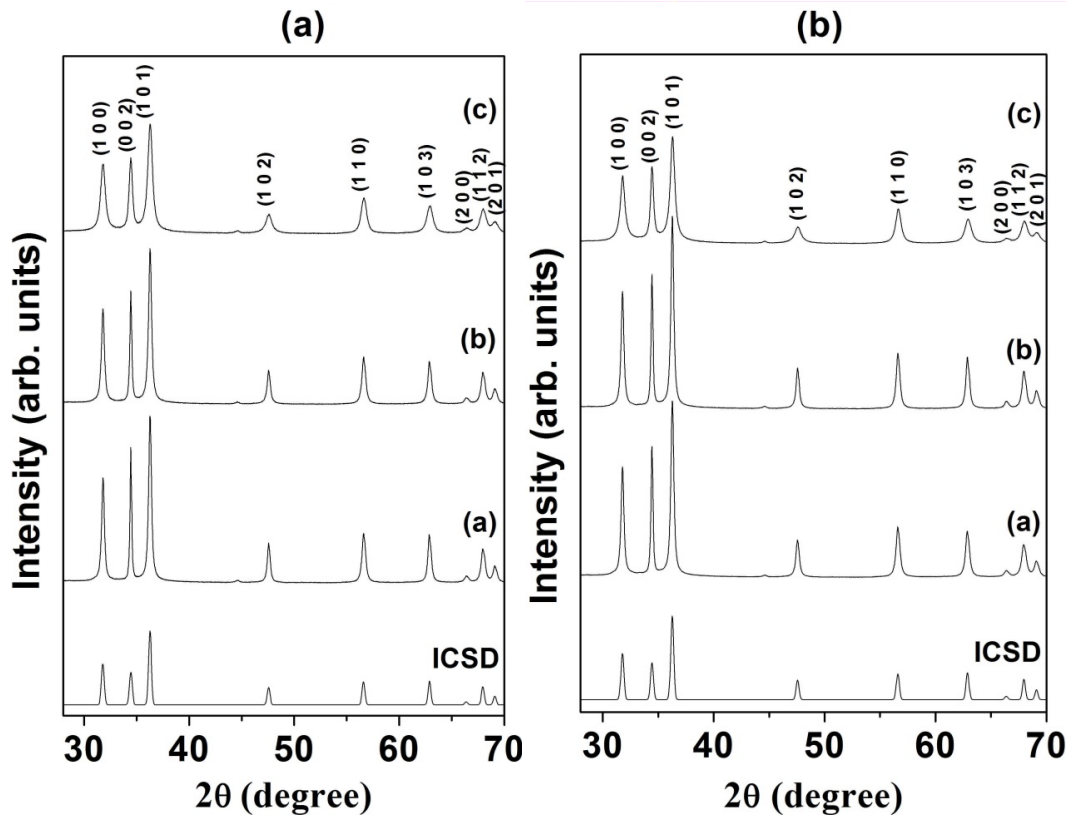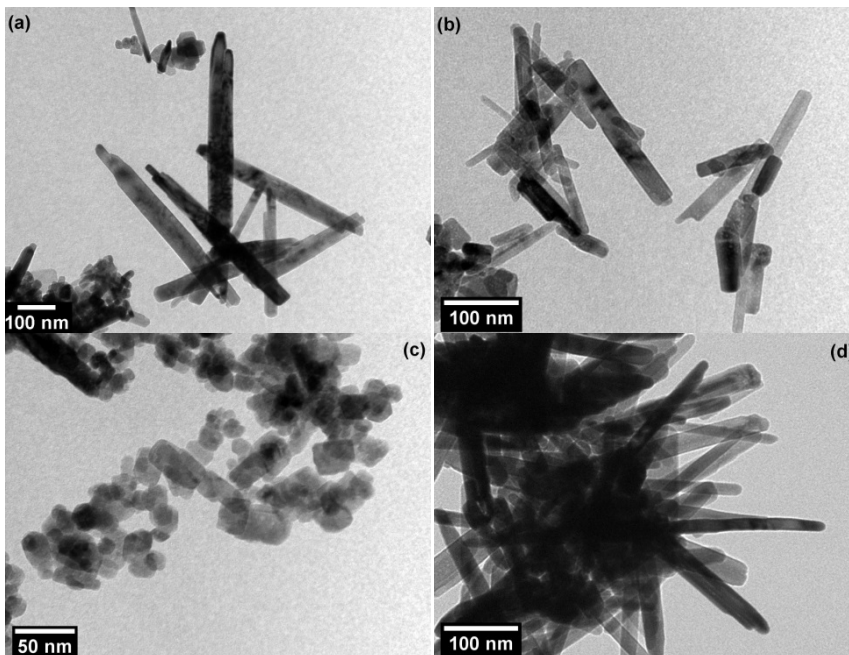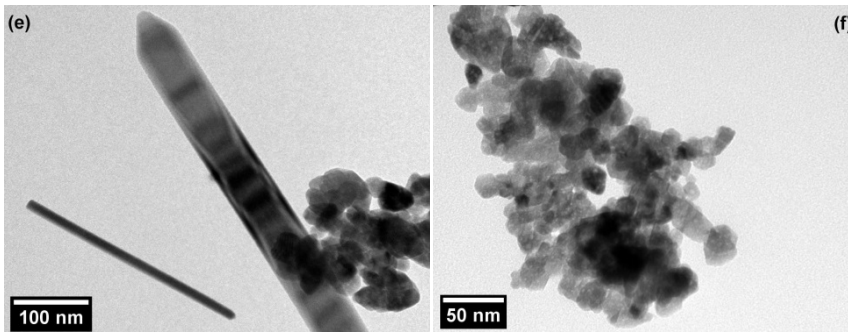

FIGURE 2.1
XRD patterns of the ZnO samples prepared with (a) zinc chloride and (b) zinc nitrate hexahydrate at different reaction temperatures: (a) 50 °C, (b) 70 °C and (c) 90 °C. Dummy pattern of the ICSD card No. 57 450 is also presented

In order to study the morphology and the size of the ZnO nanocrystals, the samples obtained by solochemical method using zinc chloride and zinc nitrate hexahydrate were investigated by TEM

(Fig. 2.2). It can be clearly observed that the ZnO samples obtained at lower reaction temperatures (50 °C and 70 °C), with both precursors, have rod-like morphology. The TEM images show that these ZnO samples are usually composed of long and short nanorods. At 90 °C, the TEM images (Fig. 2.2(c) and 2.2(f)) show that the samples obtained with different zinc precursors present similar rounded morphology and are agglomerated (especially the one formed with zinc nitrate hexahydrate).

The determination of longer and smaller sizes (defined as length and diameter, respectively) of the ZnO nanocrystals pointed out by TEM analysis was performed by measuring over more than 50 nanoparticles of several TEM images. The larger average diameters of the ZnO samples produced with zinc nitrate haxahydrate and zinc chloride were obtained at 70 °C and 50 °C, respectively. It was found that the average diameters of the ZnO samples prepared with different precursors at 50 °C do not differ considerably. This result was also observed for the samples produced at 90°C. On the other hand, at 70 °C the average diameter of the nanorods obtained with zinc nitrate hexahydrate is considerably higher than that formed with zinc chloride. The lengths of the particles synthesized at 50 °C and 70 °C are noteworthy and present average sizes above 160 nm for both zinc precursors. However, when the reaction is performed at a higher temperature, the average lengths of the ZnO samples are drastically reduced to 24 nm (zinc chloride) and 28 nm (zinc nitrate hexahydrate).
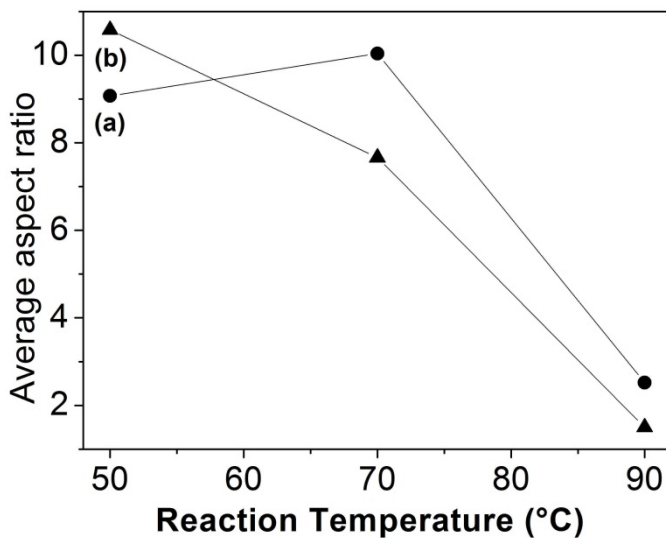
FIGURE 2.2
TEM images of the ZnO nanocrystals prepared with (a, b and c) zinc chloride and (d, e and f) zinc nitrate hexahydrate at different reaction temperatures: (a and d) 50 °C, (b and e) 70 °C and (c and f) 90 °C

Figure 2.3 shows the average aspect ratios (average length by average diameter) of the ZnO nanocrystals obtained with zinc nitrate hexahydrate (Fig. 2.3(a)) and zinc chloride (Fig. 2.3(b)) as a function of reaction temperature. The results indicate that the average aspect ratio decreases with the increase of the reaction temperature for the ZnO samples synthesized with NaOH and zinc chloride. For the materials produced with NaOH and zinc nitrate hexahydrate the average aspect ratio is remarkably higher at 70 °C than for those obtained at other reaction temperatures. However, the average aspect ratio has an abrupt reduction when the reaction is carried out at 90 °C. As it can be seen in Figure 2.3, the average aspect ratios of the ZnO nanocrystals synthesized with zinc nitrate hexahydrate at 70 °C and 90 °C are greater than those formed with $ZnCl_2$ under the same experimental conditions.

FIGURE 2.3
Average aspect ratios extracted from TEM images of the ZnO nanocrystals obtained with (a) zinc nitrate hexahydrate and (b) zinc chloride as a function of reaction temperature

Similar syntheses were carried out with identical experimental procedure using zinc chloride at a higher concentration than that used previously. However, the zinc solution concentration was kept below 0.6 M. The NaOH solution concentration was not changed. The samples synthesized with high zinc chloride concentration at different temperatures have similar X-ray diffraction patterns (Fig. 2.4) to those presented by ZnO samples obtained with lower $ZnCl_2$ concentration (Fig. 2.1(a)). Therefore, all diffraction peaks can be indexed only to the hexagonal wurtzite ZnO structure with space group $P6_3mc$ (ICSD card No. 57 450). No peaks of any other phase were detected, which indicates the high purity of the ZnO samples obtained by the solochemical processing.
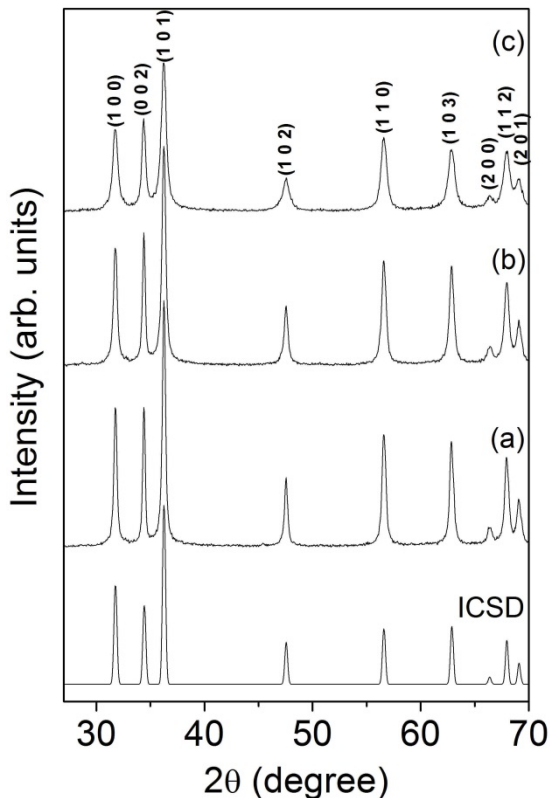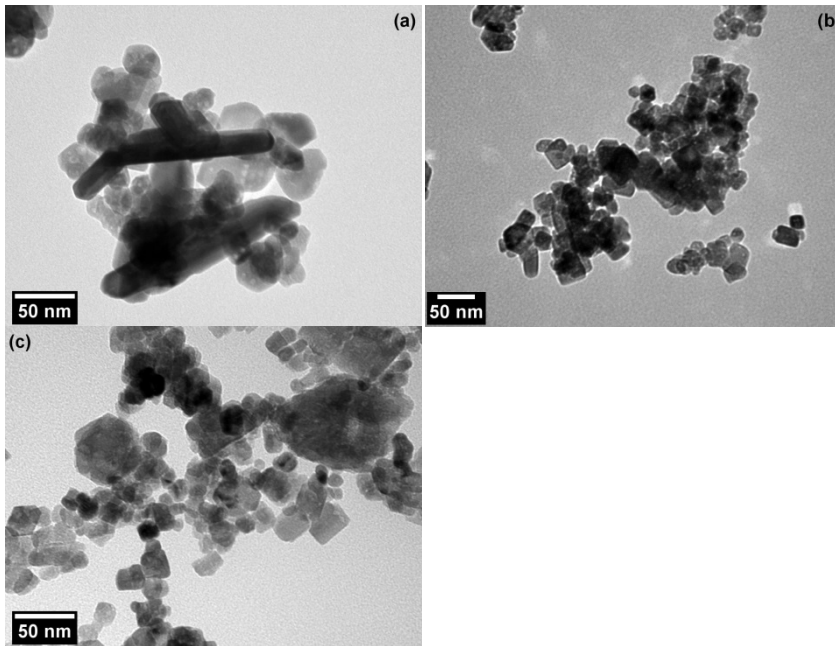

FIGURE 2.4
XRD patterns of the ZnO samples obtained with high zinc chloride concentration at different reaction temperatures: (a) 50 °C, (b) 70 °C and (c) 90 °C. Dummy pattern of the ICSD card no. 57 450 is also showed

TEM images of the ZnO samples obtained at different temperatures using high zinc chloride concentration are shown in Figure 2.5. From the TEM analysis, the ZnO samples have predominantly rod-like morphology with no considerable variation in the particles shape when compared to the ZnO nanocrystals synthesized with smaller zinc chloride concentration (Fig. 2.2(a), 2.2(b) and 2.2(c)). However, the nanorods obtained at 50 °C and 70 °C are shorter than those observed in the previous samples.
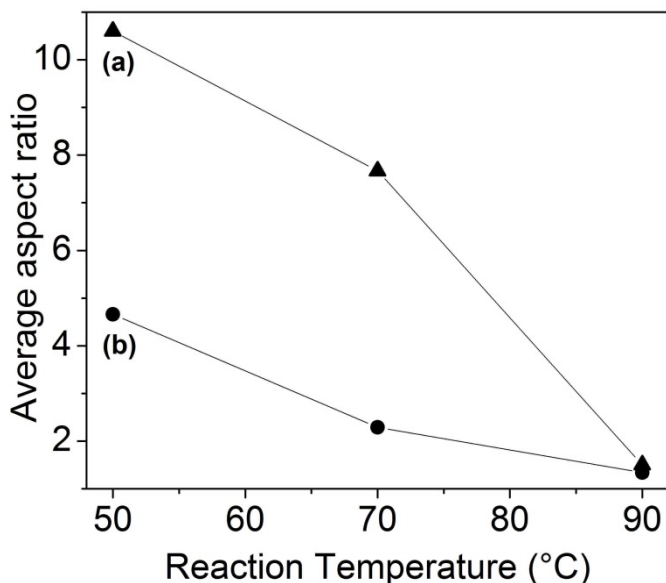
FIGURE 2.5
TEM images of ZnO nanocrystals prepared with high zinc chloride concentration at different reaction temperatures: (a) 50 °C, (b) 70 °C and (c) 90 °C

Figure 2.6 presents the average aspect ratios of the ZnO nanocrystals produced with different $ZnCl_2$ concentrations as a function of reaction temperature. It was observed that changing the zinc concentration affects significantly the size of the ZnO nanostructures, especially the length of the ZnO nanorods prepared at lower reaction temperatures. According to Figure 2.6, the average aspect ratios of the ZnO nanocrystals formed at lower zinc concentration are remarkably higher than those achieved at larger precursor concentration that applies mainly to the samples obtained at 50 °C and 70 °C.

The reaction time was also modified during the solochemical synthesis performed with NaOH and high zinc chloride concentration. Here, the duration of the reactions was five times greater than that used in the previous experiments to obtain additional information about the final size and morphology of the ZnO nanocrystals. The reactions were carried out at 50 °C and 90 °C. The products have similar XRD patterns to those of the ZnO samples prepared with a shorter reaction time (Fig. 2.1(a) and Fig. 2.4), with no indication of impurities. Therefore, the X-ray diffraction patterns of these ZnO samples showed only the characteristic peaks of the hexagonal ZnO structure according to ICSD card No. 57 450.

FIGURE 2.6
Average aspect ratios extracted from TEM images of the ZnO nanocrystals obtained with (a) low and (b) high zinc chloride concentration

Further structural characterization of the ZnO samples obtained after a long reaction time was carried out using transmission electron microscopy. The TEM images are shown in Figure 2.7. Nanorods and rounded nanoparticles can be observed in these images. Therefore, the TEM analysis of the materials showed no relevant morphological difference compared to the ZnO nanostructures synthesized with a reaction time markedly smaller (Fig. 2.5(a) and 2.5(c)). The nanocrystals obtained at 50 °C present basically long and short nanorods (Fig. 2.7(a)) with an average diameter and length of about 21 nm and 74 nm, respectively. This result shows that this sample has almost half of length of the ZnO nanocrystals prepared at the same temperature within a much shorter reaction time. When the reaction temperature is increased to 90 °C, the obtained material presents a considerable reduction in size (Fig. 2.7(b_1) and 2.7(b_2)), but their average diameter and length are very similar to those of the sample obtained with 2 h of reaction. This ZnO sample has a reasonably narrow size distribution, as shown in the histograms of Figure 2.7(b_1) and 2.7(b_2), in contrast with the ZnO sample formed at 50 °C. These observations indicate that the reaction time mainly affects the length of the ZnO particles synthesized at low reaction temperature.

Discussion

Current experiments using different precursors ($ZnCl_2$ and $Zn(NO_3)_2.6H_2O$), proved the reaction temperature to be a critical factor to the formation of ZnO nanocrystals. The results presented above showed that the particle length is the most affected parameter in the solochemical processing. It was found that the average aspect ratio of the ZnO samples tends to decrease inversely to the increase of the reaction temperature for both the zinc precursors mentioned above.   Consequently, the morphology of the ZnO samples changed from nanorods to rounded nanoparticles. The average particle length also decreases when the syntheses were performed with a higher zinc chloride concentration, or when a long reaction time was applied. Figure 2.8 shows a

schematic growth diagram of the ZnO nanocrystals based on these experimental observations. Following, the effect of different parameters on the final size and formation mechanism of the ZnO nanostructures will be discussed.

Effect of reaction temperature

In order to understand the effect of temperature over the zinc oxide nanocrystals, the solochemical reactions were performed at 50 °C, 70 °C and 90 °C using sodium hydroxide and different zinc precursors, while other experimental parameters were kept unchanged. On the basis of TEM results, it was found that the reaction temperature affects the size of the ZnO nanocrystals produced. This implies that the reaction temperature had a noticeable influence on the formation mechanism of crystals in solution, changing the nucleation and/or the growth of the ZnO particles.
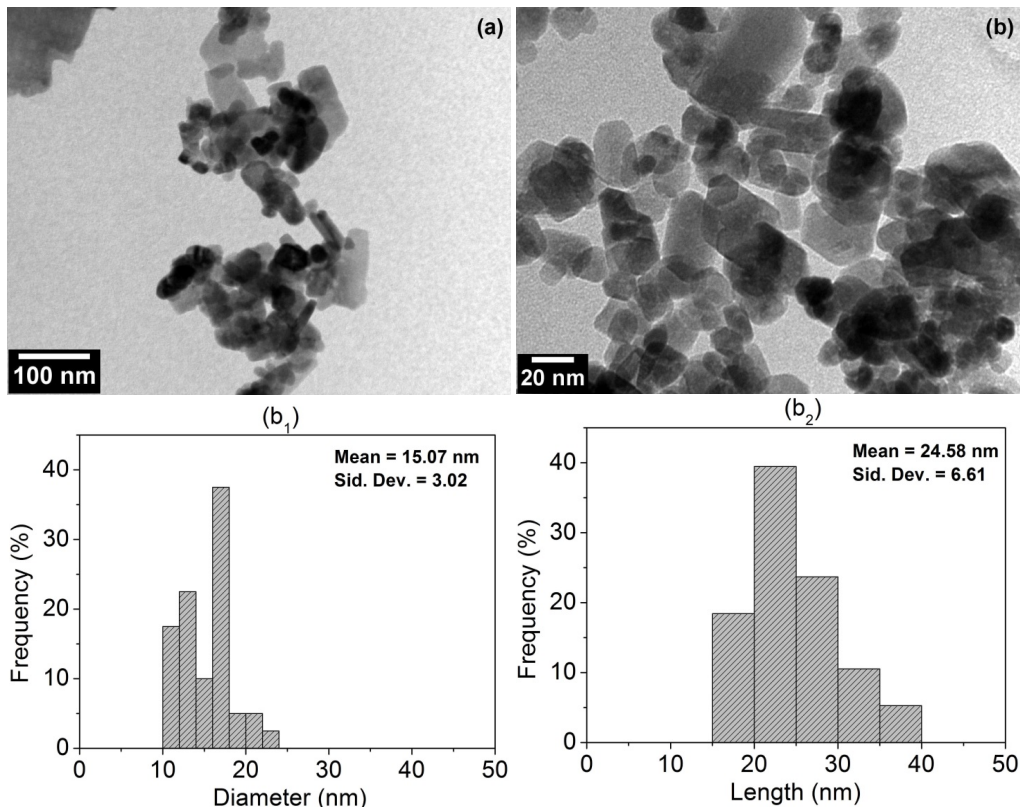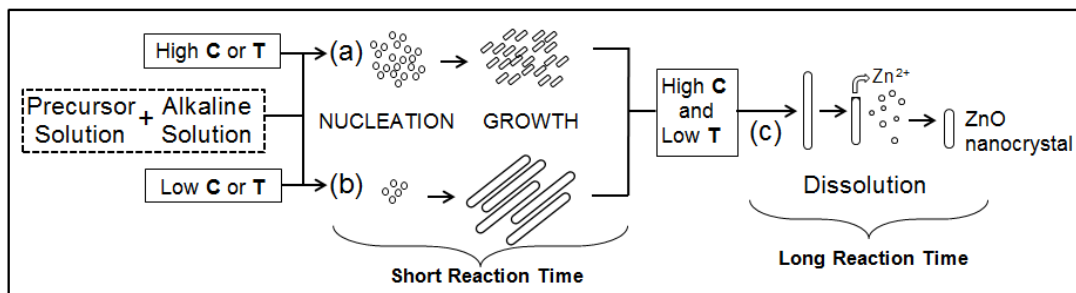

FIGURE 2.7
TEM images of ZnO nanocrystals prepared with zinc chloride at (a) 50 °C and (b) 90 °C during a reaction time of 10 h. (b$_1$) Diameter and (b$_2$) length-size histograms obtained from TEM data of ZnO nanocrystals synthesized at 90 °C are also shown

The formation mechanism of crystals in solution mainly contains the formation of growth units and the incorporation of growth units into crystal lattice of the ZnO nanocrystals [83]. At the beginning of our synthesis process, the Zn(OH)$_2$ clusters begin to develop immediately when a few drops of precursor solution (Zn(NO$_3$)$_2$.6H$_2$O or ZnCl$_2$) are added in the reactor containing the heated NaOH

solution. A high concentration of NaOH ensures proper and sufficient supply of OH⁻, which is required for the nucleation of ZnO. In an aqueous solution, the formed $Zn(OH)_2$ clusters dissolve in Zn^{2+} and OH⁻ ions due to plenty of OH⁻ ions and thermal energy (while refluxing). Thus, Zn^{2+} ions and OH⁻ ions form the $Zn(OH)_4^{2-}$ complexes [79-81], that will act in part as the basic growth units of ZnO nuclei by the dehydration of OH⁻ ions [83]. When the concentration of these growth units exceeds the critical supersaturation level, the nucleation is expected to start [84]. Therefore, the growth units become ZnO nuclei spontaneously in the solution. The nucleation rate is strongly influenced by reaction temperature and is faster at higher temperatures [85-86]. The faster the nucleation rate, the smaller the resulting particle size [87-88].

In this research, the smallest average particle sizes (length and diameter) were obtained in the syntheses performed at a higher reaction temperature with both precursors. Based on this result, we presume that in the solochemical reactions performed at 90 °C the nucleation rate is high and the formation of ZnO nuclei occurs at a faster rate. Consequently, a larger quantity of ZnO nuclei is formed which reduce the amount of growth units in the reaction medium [89-90].

The nucleation process is probably disrupted when the concentration of Zn^{2+} ions decreases in the solution [85, 87], and the particle growth is initiated. During the growth process, the incorporation of growth units into crystal lattice ceases quickly and the growth of ZnO particle is limited due to small amount of growth units in the reaction medium [89]. ZnO is a polar material and zinc and oxygen atoms are arranged alternatively along the c-axis, and the top surface is a Zn-terminated (0001) while the bottom surface is O-terminated $(000\bar{1})$. From the crystal habit of wurtzite ZnO, it is well known that the growth rate of the different planes is reported to be $(000\bar{1}) > (\bar{1}0\bar{1}1) > (1010) > (000\bar{1})$. In addition, the negative charged $Zn(OH)_4^{2-}$ complex ions are preferentially adsorbed onto the positive charged (0001) Zn face and subsequently dehydrate and enter into the ZnO crystal lattice. The growth rate along the [0001] direction is faster than those along other directions, and the more rapid the growth rate, the easier the disappearance of the plane [83, 91-92]. Thus, in the solochemical reactions, the ZnO particles growth occurs preferentially along the c-axis of wurtzite structure ([0001] direction) to form rod-like structures. Since the quantity of growth units is not enough to produce long nanorods, ZnO nanoparticles with a small final size are produced at 90 °C with both zinc precursors studied, as shown by TEM results (Fig. 2.2(c) and 2.2(f)) and in the schematic growth diagram (Fig. 2.8(a)). Similar observations were made by Wang and Muhammed [88] and Zhang et al. [93] in ZnO nanostructures obtained at low Zn^{2+} concentration and at a high pH value, respectively.

FIGURE 2.8
Schematic representation of growth mechanism of ZnO nanocrystals obtained at (a) high and (b) low temperature (T) or zinc chloride concentration (C), and (c) after 10 h of reaction

By contrast, in the syntheses performed at lower temperatures (50 °C and 70 °C) the nucleation process is slow and few nuclei are formed during the solochemical reaction. Reducing the amount of Zn^{2+} ions in the solution, possibly disrupt the formation of new nuclei. Consequently, the large amount of residual growth units, not converted in ZnO nuclei, was used for the growth of those relatively few nuclei formed. As a result, the particle growth along the [0001] direction was improved and the high aspect ratio ZnO nanorods predominated in the lower reaction temperatures for both precursors, as observed in the TEM results (Fig. 2.2(a), 2.2(b), 2.2(d) and 2.2(e)) and showed in Figure 2.8(b).

Effect of zinc precursor

The experimental results revealed that the type of zinc source also affects the size of the ZnO nanocrystals produced by the solochemical processing. Two different precursors were employed to synthesize ZnO: $Zn(NO_3)_2 \cdot 6H_2O$ and $ZnCl_2$. It was found that the morphology of the ZnO samples prepared with both zinc precursors was similar at all reaction temperatures studied. However, the average aspect ratios of ZnO nanocrystals synthesized with zinc nitrate hexahydrate at 70 °C and 90 °C are larger than those formed with $ZnCl_2$ under the same experimental conditions as it can be observed in Figure 2.3. This difference in the particle sizes can be attributed to the Cl^- ion that adsorbs more strongly on the positive polar face of the (0001) surface of the wurtzite structure of ZnO than nitrate ions, which exhibit very weak surface interaction [94].

At the beginning of the solochemical reactions, the grow units ($Zn(OH)_4^{2-}$ complexes) in the solution near the ZnO crystal are probably adsorbed on the positive charged (0001) Zn face, resulting in faster growth along the [0001] direction. When zinc chloride is used in the reactions performed at 70 °C and 90 °C, the negative ions in the solution are adsorbed preferentially on the positive polar plane (0001), which hinders the incorporation of the growth units onto this surface [95-96]. Thus, the crystal growth along the *c*-axis of ZnO structure is considerably suppressed, leading to particles with smaller sizes than those prepared with zinc nitrate hexahydrate.

Effect of zinc concentration

In this study, the experimental procedure was performed at different zinc chloride concentrations (below 0.6 M) in order to examine the function of zinc concentration in the solochemical reactions, while other parameters were left unchanged. According to Figure 2.6, the nanocrystals sizes were different when zinc chloride solutions of different concentrations were used, indicating that the precursor concentration had a strong effect on the ZnO formation. The results showed a reduction in the particle length of the ZnO nanocrystals alongside with the increase of the precursor concentration, which particularly affected the samples synthesized at 50 °C and 70 °C. Changes in the $[ZnCl_2]/[NaOH]$ ratio had lower influence on the average diameter of the ZnO nanocrystals, which slightly augmented with the increase in zinc concentration.

At the beginning of the reactions with low zinc concentration, due to the decomposition of $ZnCl_2$ and NaOH, the concentrations of Zn^{2+} and OH^- ions increased in the reaction medium. However, the ratio of Zn^{2+} to OH^- ions was possibly low in the solution due to the small amount of zinc chloride used in these experiments. As a result, the pH value of the solutions was high (~14) and it did not change during the solochemical reactions. A low Zn^{2+}/OH^- ratio favors the growth of particles with large aspect ratios [97]. Moreover, the pH controls the rate of ZnO formation and, therefore, it also affects the particle size [98]. When the pH value of the solution is high, the nucleation rate is slow, resulting in a faster growth rate [13]. Thus, when the solochemical reactions were performed with

low $ZnCl_2$ concentration in a strong alkaline aqueous medium, few nuclei were formed and the growth rate was fast due to a large amount of residual growth units in the solution. Therefore, for the reactions with low Zn^{2+}/OH^- ratio, long ZnO nanorods with large average aspect ratios were achieved, as observed in the TEM results (Fig. 2.2(a) and 2.2(b)) and in the schematic growth diagram (Fig. 2.8(b)). These observations are similar to the results of other works [92-93, 99-100].

In contrast, syntheses having increased amounts of zinc chloride formed shorter ZnO particles than the previous samples. In these reactions, the increase of precursor concentration probably caused the raise of Zn^{2+}/OH^- ratio. Li et al. [99] reported that for the reaction carried out with high Zn^{2+}/OH^- ratio, the nucleation rate is relatively fast, and the product have smaller size than that obtained from lower Zn^{2+}/OH^- ratio. According to Li et al. [87], the bigger the concentration of precursor, the smaller the resulting particle size is. Thus, when the solochemical reactions were performed with higher zinc chloride concentration, the particle formation was dominated by the production of many ZnO nuclei. After the nucleation process, the addition of growth units to the formed nuclei ceased quickly due to the small amount of growth units available in the solution [89]. As a result, shorter nanorods with low average aspect ratio were obtained in these solochemical reactions, as observed in the TEM results (Fig. 2.5 (a) and 2.5(b)) and showed in Figure 2.8(a).

It can also be seen from Figure 2.6 that the samples synthesized at 90 °C presented the lowest average aspect ratios, and the zinc concentrations did not considerably affect their particle sizes. According to Sheng et al. [92], with the increase of the reaction temperature, the release of Zn^{2+} ions is improved by the decrease of thermostabilization of the zinc complex. Hence, the nucleation rate was high even for the solochemical synthesis carried out with low zinc concentration at 90 °C, possibly due to the increase of Zn^{2+}/OH^- ratio caused by higher release of Zn^{2+} ions from the $Zn(OH)_4^{2-}$ complexes at high temperature. This result indicates that the formation mechanism of the ZnO nanocrystals synthesized at 90 °C was mainly determined by the temperature, and it had little influence of the amount of zinc chloride used in the reactions.

Effect of reaction time

After injection of zinc chloride solution into the reactor containing the heated alkaline solution, the mixture was stirred at different reaction times (2 h and 10 h) under reflux, while other parameters were kept unchanged. It was found that the average size (diameter and length) of ZnO nanorods prepared at 50 °C decreases with an increase in reaction time, which is especially true of their average lengths that were reduced from 155 nm to 74 nm. Nevertheless, the ZnO samples prepared at 2 h and 10 h in the synthesis carried out at 90 °C, showed no significant difference in their average diameters and lengths, which indicates that no further decrease in the ZnO particles size was observed above 2 h of reaction. It can be noticed from these observations that the reaction period is an important factor to control the size of the ZnO nanorods synthesized by the solochemical technique at a low temperature. The samples synthesized at 50 °C and 90 °C in a long reaction time (Fig. 2.7(a) and 2.7(b)), showed no considerable change in the particle morphology compared to those prepared with 2 h of reaction (Fig. 2.5(a) and 2.5(c)).

As it can be seen, the period in which the particles remain in the reaction media affects the size of the nanostructures obtained at 50 °C. This remark can be explained taking into account the formation mechanism of ZnO nanostructure in the solution. In the first stage of the growth process, Zn^{2+} ions react with the OH^- ions to produce $Zn(OH)_4^{2-}$ complexes. Then, the thermal decomposition of these complexes in solution leads to the production of ZnO structures. Simultaneously, ZnO can also dissolve according to the reaction 1 as the chemical equilibrium shifts toward the left [101].

$$Zn(OH)_4^{2-} \leftrightarrow ZnO + H_2O + 2OH^- \hspace{4cm} (1)$$

At the beginning of the reaction, the growth of ZnO is dominant due to high concentration of $Zn(OH)_4^{2-}$ complexes in the solution. As a result, long ZnO nanorods were obtained at 50 °C with 2 h of reaction (Fig. 2.8(b)). When the synthesis is performed during a long period, the concentration of the growth units is drastically reduced with the progress of the reaction. Moreover, at 50 °C, the decomposition reaction of the $Zn(OH)_4^{2-}$ complexes to form ZnO is almost interrupted due to low reaction temperature [102]. Thus, the reduction in the amount of growth units associated with the low temperature of the solochemical synthesis makes the dissolution process of ZnO more dominant in a long reaction time (Fig. 2.8(c)). In this case, the dissolution occurs preferentially on the positive polar face of the (0001) surface, leading to the formation of shorter ZnO nanorods than those produced in a few hours of reaction.

Polyol Method

For the past decades, the development of synthetic routes for obtaining Gd_2O_3 nanoparticles has been a subject of intense study and research given the technological and industrial significance of this material. It has been shown that the successful synthesis of these nanostructures can be achieved by several chemical processes for their low cost and reliability. Among the various chemical methods for fabrication of Gd_2O_3 nanoparticles, the polyol method is of particular interest because of its simplicity, versatility, and for being an environmentally friendly option [103]. This route is cost-effective and viable for large-scale production of Gd_2O_3 nanostructures if compared with other techniques that use complex equipment and numerous processing steps [68, 104-105].
The polyol method was first used to prepare elemental metals and alloys, in which the reducing properties of a high boiling point poly-alcohol (polyol) towards a suitable inorganic precursor were utilized [68]. This technique can also be adjusted by the addition of water to the reaction medium, which inhibits the reduction reaction, allowing oxide nanoparticles of several compounds to be obtained [106]. When water is used in the solution, forced hydrolysis and inorganic polymerization are carried out on the precursor salts dissolved in a polyol medium [106-107]. The hydrolysis reaction in this processing is remarkably fast due to the heating of the reaction mixture at high temperature (near the boiling point of polyol), which contributes to the formation of the oxides [108]. The structure and properties of the products obtained by polyol method depend mainly upon the hydrolysis ratio (defined by the water/precursor molar ratio), and reaction temperature [68, 107-109].
Typical choices of polyols include ethylene glycol, propylene glycol, and diethylene glycol (DEG) [109]. The poly-alcohols act as the solvent of the precursor salts due to its high relative permittivity [110]. They can also be the reducing agent and, in some cases, even a complexing agent [110] of said precursors. The precursor salts are suspended in the liquid polyol, in which the solids may be remarkably, or slightly soluble [111]. The resulting mixture is stirred and heated to a large temperature range up to the boiling point of the polyols [69-70] producing well-crystallized oxide nanoparticles [106-107, 112].
It must be added that the liquid polyol can act as a protective agent that avoids particles agglomeration and growth, which is the fundamental feature of the polyol method [67, 113]. The size and morphology of the nanomaterials can also be controlled by manipulating various experimental parameters such as nature and concentration of precursor, hydrolysis ratio, nature and concentration of polyol, pH of solution, reaction time, and temperature [110, 114-115]. In the

case of lanthanide oxide nanoparticles, it was found that the OH- concentration of the starting solution must not be too high in order to reduce the possibility of lanthanide hydroxide formation [116-119]. On the other hand, low OH- concentrations cause low reaction yields [120].

In the polyol process, the nucleation event occurs when the concentration of the chemical species produced during the reaction is increased quickly to the critical supersaturation level, allowing the immediate formation of nuclei [109]. The reaction temperature determines the nucleation rate that is, in turn, faster at higher temperatures [85-86]. The rapid formation of nuclei leads to a drop of the precursor concentration in the reaction medium. Consequently, the nucleation process is disrupted and the growth of particles is started from the formed nuclei. Given that the polyol itself can limit the growth process of the particles, the formation of materials at nanoscale is favored. Generally, when the nucleation and growth processes are well-controlled, the products obtained by polyol method consist of non-agglomerated and spherical particles with a narrow size distribution [109]. Therefore, this approach appears to be a versatile route to produce different materials in a wider variety of sizes.

Here, gadolinium oxide nanoparticles were obtained by direct precipitation in a high boiling point alcohol using diethylene glycol. In a typical synthesis, appropriate quantity of gadolinium nitrate hexahydrate ($Gd(NO_3)_3 \cdot 6H_2O$) is added to diethylene glycol and then the mixture is heated to 100 °C for complete dissolution of the gadolinium precursor. After a clear solution is formed under vigorous magnetic stirring, a sufficient volume of NaOH aqueous solution of high basicity is added into the reactor containing the precursor. The emerging suspension is heated up to 140 °C for 1 h. Then, the mixture is heated up to 170 °C and maintained at this temperature for 4 hours. After the reaction is completed, the suspension is processed by centrifugation, washing using methanol, and drying at vacuum oven in order to obtain the amorphous powder product (sample A). Subsequent calcination of this product was made at high temperatures for 5 h to produce Gd_2O_3 nanoparticles. The additional thermal treatments for the sample A were carried out at 850 °C (sample B) and 900 °C (sample C).

Figure 2.9 shows the XRD patterns of the material obtained by polyol route before and after calcination at 850 °C and 900 °C. Figure 2.9(a) shows that before the thermal treatment, sample A is predominantly amorphous. Only the very broad (222) peak, due to Gd_2O_3 crystals, can be observed in the XRD pattern. After thermal treatment at 850 °C and 900 °C, the diffraction peaks (Fig. 2.9(b) and 2.9(c)) become sharp and prominent which indicate the improvement of material crystallinity. The calcined samples have similar XRD patterns and all diffraction peaks can be indexed to the cubic phase of Gd_2O_3 with space group Ia_3 (ICSD card No. 40 473). Since no extra diffraction peaks were observed in the XRD patterns of samples B and C, it is concluded that pure Gd_2O_3 structures were synthesized through this simple polyol method after thermal treatment.

The diffraction peaks of Gd_2O_3 samples obtained after calcination have significant line broadening, which indicates that the crystal sizes are most likely in the nanometer range. Making use of the most prominent characteristic (222) peak, the average crystallite size of the calcined samples is estimated using the Scherrer's equation ($D = k.\lambda / \beta.cos\vartheta$, k = 0.99 for spherical particles) [121-122]. It was confirmed that the average crystallite sizes of the Gd_2O_3 samples calcined at 850 °C and 900 °C indeed lie in the nanometer range and are about 25 nm and 36 nm, respectively. These results show that the average crystallite size of the gadolinium oxide nanocrystals increases with a rise in calcination temperature.

The TEM images of the Gd_2O_3 nanocrystals prepared by the polyol method before and after heat treatment at different temperatures are shown in Figure 2.10. The TEM image of the material obtained before calcination shows some rounded particles with a considerable degree of

agglomeration. After thermal treatment of sample A, quasi-spherical Gd_2O_3 nanoparticles of nearly uniform size were observed in the TEM images (Fig. 2.10(b) and 2.10(c)).

In order to quantify the size of the Gd_2O_3 nanocrystals pointed out by TEM analysis, over 50 particles of several TEM images were measured. The average diameter of the Gd_2O_3 nanocrystals obtained after calcination at 850 °C is about 24 nm and the sample's size ranges between 18 nm and 31 nm. The Gd_2O_3 particles formed after thermal treatment at 900 °C presented a size ranging from 20 nm to 46 nm and an average diameter of around 31 nm. The results show that the average particle size tends to increase with the rise of the calcination temperature. These findings are in good agreement with the average crystallite sizes calculated from the XRD data. The average sizes obtained in this study are larger than those previously reported average diameters for the synthesis of Gd_2O_3 nanoparticles using the polyol method with DEG [119, 123-125]. The selected area electron diffraction (SAED) pattern (Fig. 2.10(d)) suggests that the Gd_2O_3 nanostructures obtained after calcination at 900 °C are crystalline in nature.
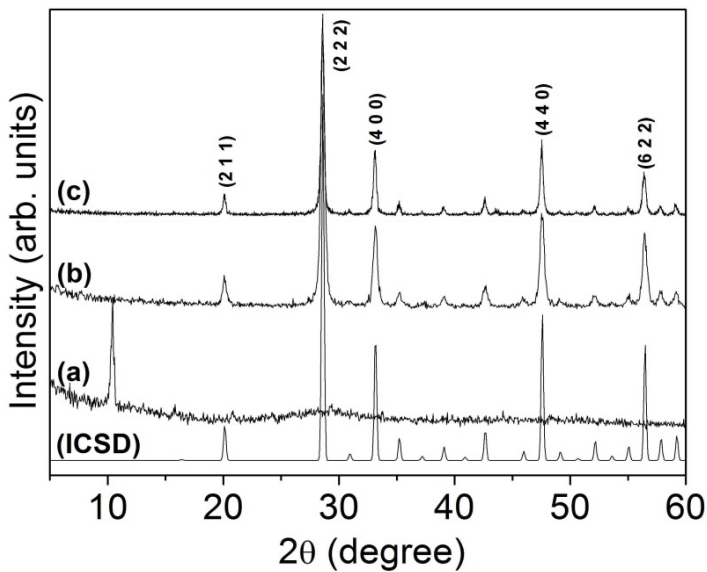
FIGURE 2.9
XRD patterns of Gd_2O_3 samples prepared by the polyol method (a) before and after thermal treatment at (b) 850 °C and (c) 900 °C. Dummy pattern of the ICSD card No. 40 473 is also presented
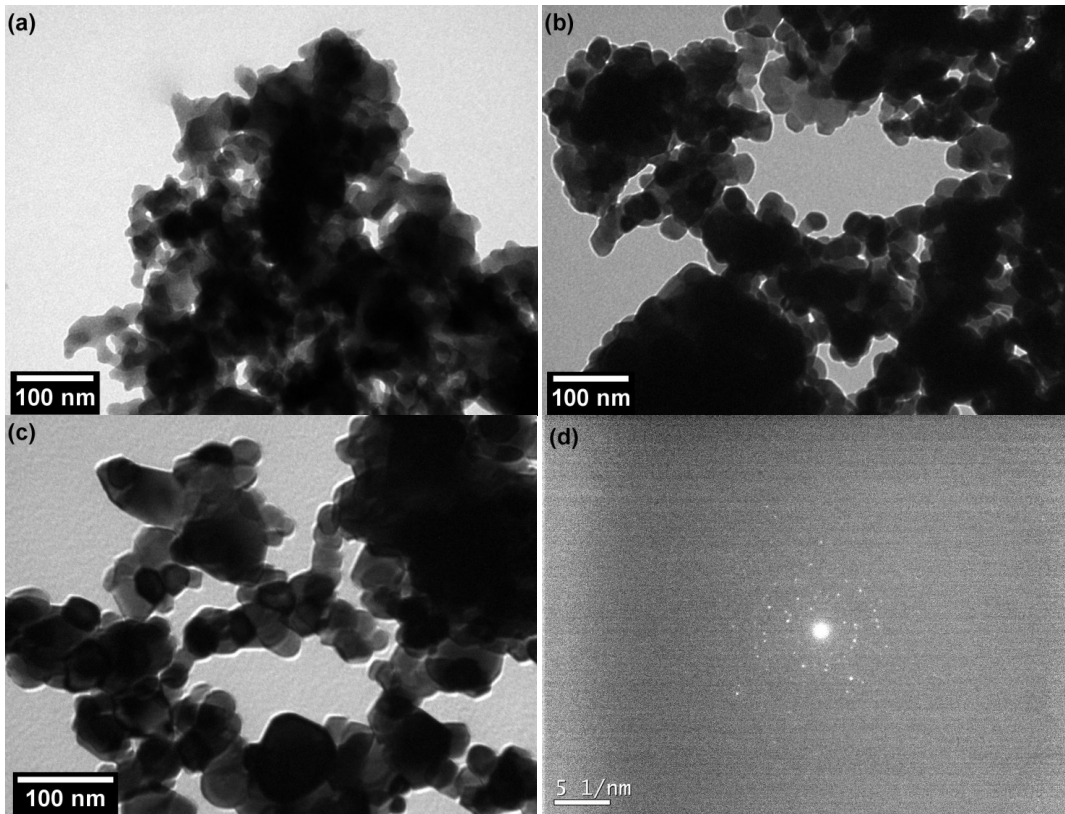
FIGURE 2.10
TEM images of Gd$_2$O$_3$ nanocrystals (a) before and after thermal treatment at (b) 850 °C and (c) 900 °C; (d) Selected area electron diffraction (SAED) pattern recorded from the Gd$_2$O$_3$ nanoparticles obtained after calcination at 900 °C

Sol-gel Process

Among the various chemical routes, the sol-gel method is the most used procedure in the preparation of glasses and ceramics [126]. The sol-gel method produces a wide variety of inorganic oxide materials with interesting properties, and it has also proved to be a viable technique for the synthesis of various oxide nanomaterials [127-130]. The sol-gel process can be used under mild reaction conditions and it allows for the obtaining of products of various sizes and shapes (monoliths, films, fibers, powder, spheres) [126, 129, 131]. The sol-gel technique has many advantages such as process simplicity, high stability, better homogeneity, high purity, stoichiometry control, and low processing temperature [126, 132-134]. However, some disadvantages include the high cost of the starting materials, and the formation of generally amorphous products, which require subsequent thermal treatments at high temperatures to prompt the crystallization process [134-135].

In the aqueous sol-gel process, the conversion of a precursor solution into an inorganic solid is triggered by water [136]. In general, the precursor or starting compound is either an inorganic

metal salt, or a metal organic compound such as an alkoxide. Metal organic compound is the most extensively used precursor in sol-gel reactions once it reacts readily with water [137-138]. The choice for alkoxides was due to their ability to control the hydrolysis rate with the addition of alcohols [129]. The reaction can be catalyzed with the addition of either an acid or a base in the solution [129].

The general principles of sol-gel process have been extensively studied and describes in the literature [126, 134, 139]. In general, the sol-gel method involves the following main stages [139]: i) formation of a homogeneous solution through the dissolution of metal organic compounds in an organic solvent, or by the dissolution of inorganic metal salts in water; ii) conversion of the homogeneous solution into a sol, which can be defined as a colloidal suspension of solid particles (with diameters of 1-100 nm [140]) in a liquid phase; iii) gelation; iv) aging; v) drying; and vi) thermal treatment.

The first two stages in the sol-gel processing consist in manufacturing networks of inorganic elements, which are obtained through a chemical process that starts from a hydrolysis reaction of precursors, and continues through condensation reactions. Said process would result in a homogeneous colloidal dispersion with low viscosity called sol [141]. Throughout this step, different parameters affect the hydrolysis rate. Such parameters are: temperature, nature and concentration of the precursor, pH value, and type of solvent used in the sol-gel reaction [129]. The pH value of the sol alters substantially the structure of the particles and the properties of the formed materials, once it influences the hydrolysis and condensation reactions [142].

As the hydrolysis and condensation reactions continue, the colloidal particles (sol) link together resulting in gelation, and forming a structure with macroscopic size called gel [136]. During this stage, there is a remarkable increase in the viscosity of the solution as the sol is transformed into a gel [143]. The time for gelation is dependent on the precursor concentration and the structure of the alcohol used [129]. The gel is an interconnected, rigid, and porous polymeric network enclosing a continuous liquid phase [144].

In the aging step, the structure and properties of the gel network continue to be modified, leading to variation in the pH value at the liquid phase, which probably influences the gelation process [145]. Aging consists in the contraction of the gel network and expulsion of liquid (solvent and water) from the gel pores to allow further solidification [146]. During this process, the polycondensation reactions continue to occur, transforming the gel into a cross-linked structure. At this stage, parameters such as time, solvent, type of aged sol-gel, and pH value affect the size and crystal structure of the formed nanoparticles [145-146]. The temperature also influences the aging step. At lower temperatures, the resulting gel is more flexible, but at higher temperatures, the condensation reactions are very fast, making the gel structure more rigid [129].

Another important step in the sol-gel processing is the drying, when hydrolysis and gelation may also occur [145]. Drying of the gel consists on the final removal of the liquid phase from the interconnected pore network [147]. This stage involves various processes, such as evaporation of water occluded into the gel, solvent evaporation, elimination of organic residues, and structural and micro-structural changes [148]. Large stresses can develop during this phase, which may cause the crack of the gel if the drying process is not controlled [144]. Several techniques have been developed to prevent collapse of the network, including supercritical drying [143]. In this case, the liquid is removed as a gas phase from the interconnected solid gel network under supercritical conditions, reducing thus the stresses and producing an aerogel [129]. When the gel is dried at, or near ambient conditions it turns into a solid known as xerogel [147].
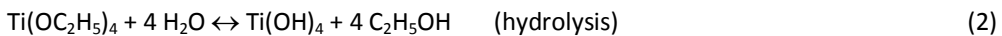
The dried xerogel or aerogel should be thermally converted into a more active and stable solid phase [136]. During the thermal treatment (annealing, sintering, and/or calcination), the materials

are subjected to high temperatures [145], which generates modifications in the geometry and crystal structure of the materials [146, 149]. When the materials are thermal treated, the alkyl and hydroxyl groups are removed, resulting in additional shrinkage of the solid matter [146]. In general, high calcination temperature and a long thermal treatment time produce a material with a perfect crystal structure, high crystallinity, and larger particle size [145].
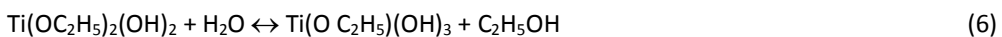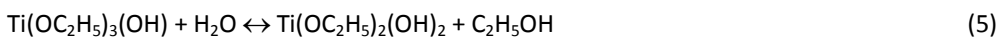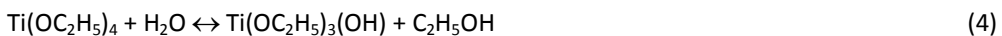
Therefore, the sol-gel method is a very interesting solution-based synthetic technique for the low-temperature preparation of oxide nanomaterials. Under controlled preparation conditions, depending on the nature of the precursors, the use of surfactants, acid or base catalysis, and the water/precursor and cosolvent/precursor ratios, nanocrystalline products with high purity level can be produced [150-151].

The sol-gel technique has been widely applied for preparing titanium dioxide (TiO_2) nanoparticles due to the fact that this processing allows an easy control of the hydrolysis and condensation reactions [131, 152]. In a typical sol-gel synthesis of titanium dioxide nanoparticles [153], a given amount of deionized water was dissolved in dry ethanol (C_2H_5OH) to form an aqueous solution. This solution was heated while stirred inside a reactor. Once the aqueous solution reached the desired reaction temperature (80 °C), the precursor solution prepared with $Ti(OC_2H_5)_4$ (titanium ethoxide) and dry ethanol was slowly transferred to the reactor. During this step, no significant change in the temperature was observed. After injection, the previously transparent mixture acquires white coloring indicating the formation of TiO_2 nanostructures. The resulting mixture was stirred for 2 h and the refluxing temperature was kept at the same value chosen at the beginning of the reaction. The product was filtered and washed with deionized water, and then dried at 90 °C for several hours in order to obtain the amorphous product. Two different samples will be formed using this procedure by changing the hydrolysis ratio (r = [H_2O]/[Ti(OR)$_4$]) of the process. The water/alkoxide ratios used in these syntheses were r = 15 (A-TiO_2 sample), and r = 100 (B-TiO_2 sample). Subsequent calcination of the samples was made at 500 °C for different hours to form the TiO_2 nanoparticles.

TiO_2 nanostructures have been successfully formed through the hydrolysis and condensation reactions of titanium ethoxide in the aqueous media. In the presence of water, the alcoxide is hydrolyzed and subsequently polymerized to form a interconnected oxide network. According to the literature [154], these reactions can be schematically represented as follows:

$Ti(OC_2H_5)_4 + 4 H_2O \leftrightarrow Ti(OH)_4 + 4 C_2H_5OH$ (hydrolysis)   (2)

$Ti(OH)_4 \leftrightarrow TiO_2 (s) + 2 H_2O$ (condensation)   (3)

The hydrolysis reaction has four possible intermediate steps that are:

$Ti(OC_2H_5)_4 + H_2O \leftrightarrow Ti(OC_2H_5)_3(OH) + C_2H_5OH$ (4)

$Ti(OC_2H_5)_3(OH) + H_2O \leftrightarrow Ti(OC_2H_5)_2(OH)_2 + C_2H_5OH$ (5)

$Ti(OC_2H_5)_2(OH)_2 + H_2O \leftrightarrow Ti(O C_2H_5)(OH)_3 + C_2H_5OH$ (6)

$Ti(OC_2H_5)(OH)_3 + H_2O \leftrightarrow Ti(OH)_4 + C_2H_5OH$ (7)

The condensation reaction moves forward through a water (Eq. 8), or alcohol (Eq. 9) elimination reaction.

$$Ti\text{-}OH + HO\text{-}Ti \leftrightarrow Ti\text{-}O\text{-}Ti + H_2O \tag{8}$$

$$Ti\text{-}OC_2H_5 + HO\text{-}Ti \leftrightarrow Ti\text{-}O\text{-}Ti + C_2H_5OH \tag{9}$$

Thus, the reaction of TiO_2 formation is initiated by hydrolysis of the alkoxide, in which the $-OC_2H_5$ group is replaced via the nucleophilic attack of the oxygen atom of a water molecule, with the transfer of a proton from water to the alkoxide group, under release of the resulting alcohol molecule (C_2H_5OH) [136, 155]. In the second step, the condensation reaction brings together the constituent particles of the gel into a solid mass, thereby forming the metal oxide material [156]. After gelation, the formed product is dried and calcined so as to remove the organic molecules from the final TiO_2 and complete the crystallization process.
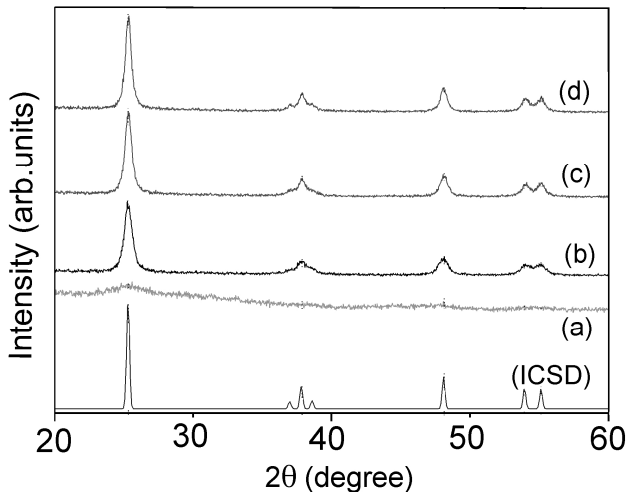
Figure 2.11 shows the XRD patterns of the A-TiO_2 sample prepared with a hydrolysis ratio of $r = 15$ before and after thermal treatment at 500 °C during 1 h, 3 h and 6 h. The XRD pattern (Fig. 2.11(a)) shows that before thermal treatment the A-TiO_2 sample is amorphous. Upon being calcined for 1 h, the product became crystalline and was found to consist of anatase phase (ICSD card No. 94 566) with a small diffraction peak at 30.8° corresponding to the brookite phase of TiO_2 [157] (Fig. 2.11(b)). The XRD patterns of the A-TiO_2 sample calcined during 3 h and 6 h (Fig. 2.11(c) and 2.11(d)) show that all diffraction peaks can be explained only by the anatase phase of TiO_2. Figure 2.11 shows that the calcination time considerably improves the crystallinity of the material.
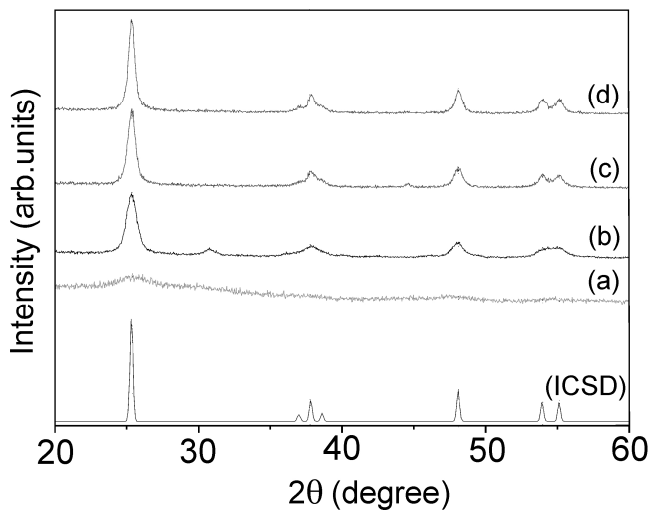
FIGURE 2.11
XRD patterns of the A-TiO_2 sample prepared with $r = 15$ by sol-gel process (a) before and after thermal treatment for (b) 1 h, (c) 3 h and (d) 6 h [153]. Dummy pattern of the ICSD card No. 94 566 is also presented

The XRD patterns of the B-TiO_2 sample prepared using $r = 100$ before and after heat treatment at different times are shown in Figure 2.12. For this hydrolysis ratio value, all XRD patterns of the samples calcined at different times (Fig. 2.12(b), 2.12(c) and 2.12(d)) are similar and can be indexed only by the anatase phase of TiO_2 (ICSD card No. 94 566). Therefore, the XRD results of the A-TiO_2 and B-TiO_2 samples indicate that the water/alkoxide ratio and calcination time have significant effects on the crystalline phase of TiO_2 prepared by the sol-gel method.

FIGURE 2.12
XRD patterns of the B-TiO$_2$ sample prepared using r = 100 by sol-gel method (a) before and after calcination for (b) 1 h, (c) 3 h and (d) 6 h [153]. Dummy pattern of the ICSD card No. 94 566 is also presented

The XRD patterns of the A-TiO$_2$ and B-TiO$_2$ samples, obtained at different hydrolysis ratios, were refined by Rietveld method considering the anisotropic model for determination of crystallite sizes using GSAS formalism [158-159]. In this model, each crystallite is regarded as having its own lattice parameters, with multidimensional distribution throughout the powder sample. The width of each reflection can be expressed in terms of moments of this distribution, which leads naturally to parameters that can be varied to achieve optimal fits, as shown in Figure 2.13(a) and 2.13(b) for the A-TiO$_2$ and B-TiO$_2$ samples, respectively.
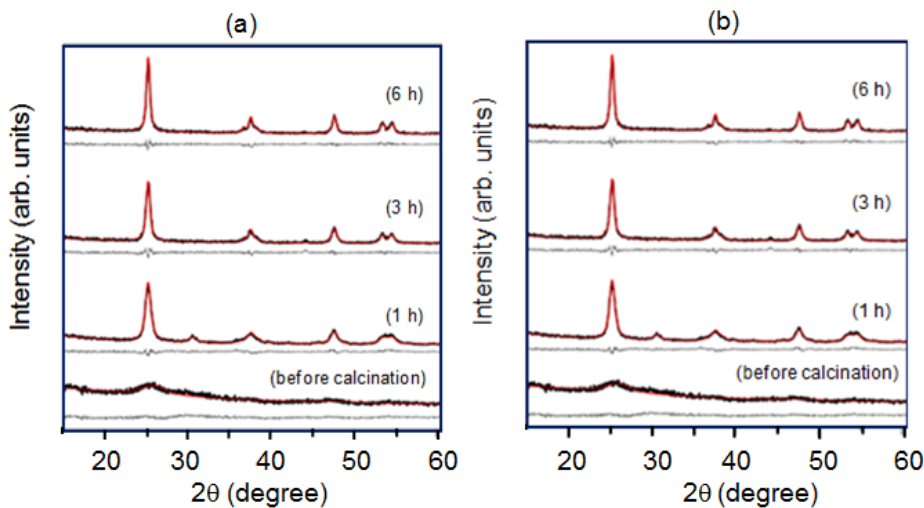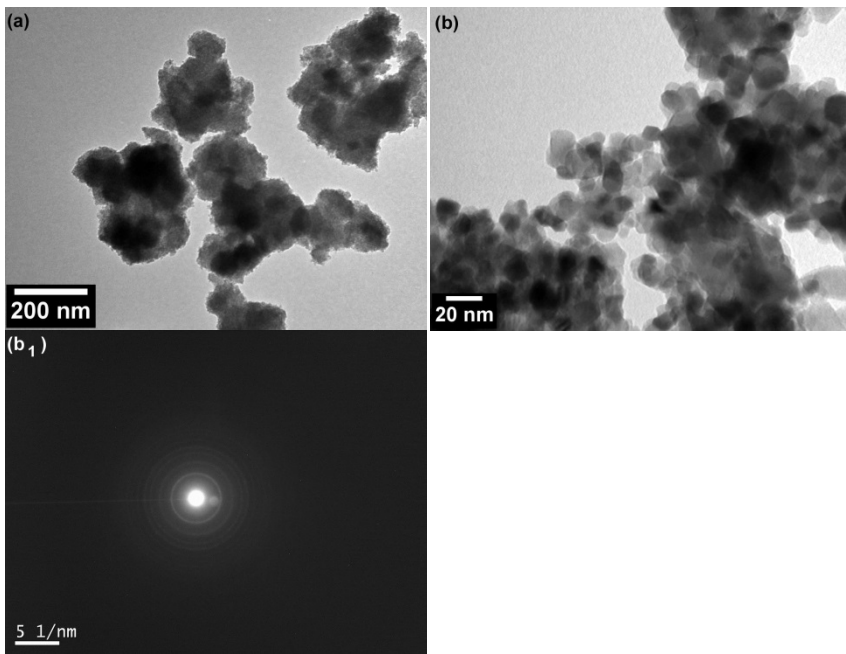

FIGURE 2.13
Experimental (black lines) and calculated (red lines) XRD patterns of the (a) A-TiO$_2$ and (b) B-TiO$_2$ samples produced by the sol-gel method before and after calcination at different times; gray lines represent the difference between experimental and calculated patterns [153]

The average crystallite sizes obtained from Rietveld analysis for the A-TiO$_2$ sample calcined at 3 h and 6 h were 16.27 nm and 18.74 nm [153], respectively. The average crystallite sizes of the sample synthesized with a higher hydrolysis ratio and then heat treated for 3 h and 6 h showed no significant differences with respect to A-TiO$_2$ sample (17.53 nm and 20.02 nm [153], respectively). These results show that the average crystallite size rises with increasing calcination time.

The TEM images and the select area electron diffraction (SAED) pattern of the A-TiO$_2$ sample, prepared by sol-gel process before and after calcination for 6 h, are shown in Figure 2.14. The TEM image of the calcined sample (Fig. 2.14(b)) indicates that the TiO$_2$ nanoparticles are almost spherical in shape. From the TEM analysis, the near spherical particles have an estimated average diameter of about 14 nm. This result is in good agreement with the average crystallite size of the A-TiO$_2$ sample determined by Rietveld analyses. The SAED image suggests a high crystalline nature of the TiO$_2$ nanoparticles prepared by sol-gel process after thermal treatment for 6 h (Fig. 2.14(b$_1$)).

FIGURE 2.14
TEM images of the TiO$_2$ nanoparticles obtained (a) before and after thermal treatment at 500 °C for (b) 6 h; (b$_1$) SAED pattern of the A-TiO$_2$ sample obtained after calcination at 500 °C for 6 h is also shown [153]

Conclusion

In this chapter, simple, fast, and cost-effective methods to synthesize different nanomaterials with a very high level of chemical purity have been presented. Zinc oxide nanocrystals were produced by the solochemical processing under mild reaction conditions. The ZnO nanostructures were prepared with no pretreatment of the reactants and no calcination process after the drying step of the samples. Moreover, no surfactant, capping agent, or other additives were added into the reaction medium. Controllable growth of ZnO nanocrystals is feasible by using different kinds of

zinc sources, temperatures, precursor concentrations, and reaction times. It was revealed by TEM analysis that ZnO nanocrystals presented predominantly rod-like morphology and large aspect ratio when the reactions were performed at 50 °C and 70 °C, with both zinc precursors. Higher average size ratios were also obtained using a lower zinc chloride concentration (50 °C and 70 °C) as well as when a shorter reaction time was applied (50 °C). At 90 °C, the ZnO samples presented the smallest average size (diameter and length) and a rounded shape for all reactions conditions studied.

Gd_2O_3 nanoparticles were successfully prepared through a facile polyol technique and subsequent calcination process. This simple method has been demonstrated as an economical and effective technique for the synthesis of Gd_2O_3 nanostructures. The Gd_2O_3 nanoparticles showed predominantly spherical morphology for both calcination temperatures studied (850 °C and 900 °C). Besides, the calcination temperature has been found to play a crucial role in tuning the size of the Gd_2O_3 nanoparticles. The TEM analysis showed that after thermal treatment, the Gd_2O_3 samples' size increased as the calcination temperature increased.

Finally, the sol-gel method described in the present chapter has been successfully used to synthesize titanium dioxide nanoparticles. This technique proved to be a convenient synthetic route for production of TiO_2 nanostructures in terms of cost, ease of handling, reliability, and mild reaction conditions. By varying the reaction conditions, such as hydrolysis ratio and/or calcination time, it is possible to obtain anatase or brookite (A-TiO_2 sample calcined for 1 h) phase of TiO_2. Moreover, the Rietveld analysis showed that the average crystallite size is affected by the calcination time, and it rises with increasing heat treatment time. It was revealed by TEM results that the TiO_2 sample obtained after thermal treatment at 500 °C for 6 h has almost spherical shape with an average diameter of about 14 nm.

Acknowledgment

References

1. A. P. Alivisatos, Science 271, 933 (1996).
2. X. Gao, X. Li, W. Yu, J. Solid State Chem. 178, 1139 (2005).
3. J. Y. Lao, J. Y. Huang, D. Z. Wang, Z. F. Ren, Nano. Lett. 3, 235 (2003).
4. Z. Yang and Q.-H. Liu, Physica E 40, 531 (2008).
5. J. Du, Z. Liu, Y. Huang, Y. Gao, B. Han, W. Li, G. Yang, J. Cryst. Growth 280, 126 (2005).
6. C. Pacholski, A. Kornowski, H. Weller, Angew. Chem. Int. Ed. 43, 4774 (2004).
7. C. Wang, Q. Li, B. Mao, E. Wang, C. Tian, Mater. Lett. 62, 1339 (2008).
8. L. Castaneda, Acta Mater. 57, 1385 (2009).
9. X. Han, G. Wang, Q. Wang, L. Cao, R. Liu, B. Zou, J. G. Hou, Appl. Phys. Lett. 86, 223106 (2005).
10. X. Y Kong and Z. L.Wang, Nano. Lett. 3, 1625 (2003).
11. J. Y. Lao, J. Y. Huang, D. Z. Wang, Z. F. Ren, D. Steeves, B. Kimball, W. Porter, Appl. Phys. A 78, 539 (2004).
12. W. I. Park, G. C. Yi, M. Kim, S. J. Pennycook, Adv. Mater. 14, 1841 (2002).

13. U. Pal and P. Santiago, J. Phys. Chem. B 109, 15317 (2005).
14. S. C. Minne, S. R. Manalis, C. F. Quate, Appl. Phys. Lett. 67, 3918 (1995).
15. S. Music´, S. Popovic´, M. Maljkovic, Đ. Dragcevic´, J. Alloys Compd. 347, 324 (2002).
16. E. A. Meulenkamp, J. Phys. Chem. B 102, 5566 (1998).
17. Y. Fangli, H. Peng, Y. Chunlei, H. Shulan, L. Jinlin, J. Mater. Chem. 13, 634 (2003).
18. W. Li, S. I. Shah, C. P Huang, O. Jung, C. Ni, Mater. Sci. Eng. B96, 247 (2002).
19. K. P. Priyanka, S. Joseph, S. Thankachan, E. M. Mohammed, T. Varghese, J. Basic Appl. Phys. 2, 4 (2013).
20. W. Li, C. Ni, H. Lin, C. P. Huang, S. I. Shah, J. Appl. Phys. 96, 6663 (2004).
21. M.-I. Baraton, T. O. Nano. J. 5, 64 (2011).
22. K. Kalyanasundaram and M. Gratzel, Efficient photovoltaic solar cells based on dye sensitization of nanocrystalline oxides films, In: D. M. Roundhill and J. P. Fackler Jr. (ed.), Optoelectronic properties of inorganic compounds, Series: Modern Inorganic Chemistry, Plenum, New York, p. 169-192, (1999).
23. P. Bonhole, E. Gogniat, M. Gratzel, P. V. Ashrit, Thin Solid Films 350, 269 (1999).
24. G. Sheveglieri, Gas sensors, Kluwer, Dordrecht (1992).
25. H. Selhofer, Vac. Thin Films 2, 15 (1999).
26. A. Fujishima, T. N. Rao, D. A. Tryk, J. Photochem. Photobiol. C: Photochem. Rev. 1, 1 (2000).
27. R. Zallen, M. P. Moret, Solid State Commun. 137, 154 (2006).
28. Y. Sakatani, D. Grosso, L. Nicole, C. Boissiere, G. J. A. A. Soler-Illia, C. Sanchez, J. Mater. Chem. 16, 77 (2006).
29. C. Hu, Y. Lan, X. Hu, A. Wang, J. Phys. Chem. B, 110, 4066 (2006).
30. K. Pirkanniemi and M. Sillanpaa, Chemosphere 48, 1047 (2002).
31. G. Centi, P. Ciambelli, S. Perathoner, P. Russo, Catalysis Today 75, 3 (2002).
32. D. B. Chu, X. H. Li, X. Y. Liu, W. L. Yao, Chin. J. Chem. 22, 1231 (2004).
33. C. M. Ronconi and E. C. Pereira, J. Appl. Electrochem. 31, 319 (2001).
34. S. J. W. Shi, S. H. Chen, S. M. Wang, P. Wu, G. H. Xu, J. Mol. Catal. A: Chem. 303, 141 (2009).
35. M. Zhou, J. Yu, H. Yu, J. Mol. Catal. A: Chem. 313, 107 (2009).
36. G. Magesh, B. Viswanathan, R. P. Viswanath, T. K. Varadarajan, Indian J. Chem. 48A, 480 (2009).
37. S. Hu, F. Li, Z. Fan, Bull. Korean Chem. Soc. 33, 1269 (2012).
38. J. E. Canas, B. Qi, S. Li, J. D. Maul, S. B. Cox, S. Das, M. J. Green, J. Environ. Monit. 13, 3351 (2011).
39. C. Suzuki, J. Kawai, M. Takahashi, A.-M. Vlaicu, H. Adachi, T. Mukoyama, Chem. Phys. 253, 27 (2000).
40. J. Yang, C. Li, Z. Quan, C. Zhang, P. Yang, Y. Li, C. Yu, J. Lin, J. Phys. Chem. C 112, 12777 (2008).
41. M. Jayasimhadri, B. V. Ratnam, K. Jang, H. S. Lee, B. Chen, S.-S. Yi, J.-H. Jeong, L. R. Moorthy, J. Appl. Ceram. Technol. 8 709 (2011).
42. H. Guo, N. Dong, M. Yin, W. Zhang, L. Lou, S. Xia, J. Phys. Chem. B 108, 19205 (2004).
43. H. Guo, X. Yang, T. Xiao, W. Zhang, L. Lou, J. Mugnier, Appl. Surf. Sci. 230, 215 (2004).
44. S. Yue, F. Wei, Y. Wang, Z. Yang, J. Du, J. Phys.: Conf. Ser. 152, 012004 (2009).
45. N. C. Das, N. K. Sahoo, D. Bhattacharyya, S. Thakur, D. Nanda, S. Hazra, J. K. Bal, J. F. Lee, Y. L. Tai, C. A. Hsieh, J. Appl. Phys. 110, 063527 (2011).

46. M. P. Singh, C. S. Thakur, K. Shalini, S. Banerjee, N. Bhat, S. A. Shivashankar, J. Appl. Phys. 96, 5631 (2004).
47. N. K. Sahoo, M. Senthilkumar, S. Thakur, D. Bhattacharyya, Appl. Surf. Sci. 200, 219 (2002).
48. A. T. M. A. Rahman, K. Vasilev, P. Majewski, J. Colloid Interface Sci. 354, 592 (2011).
49. A. Alemi, S. W. Joo, S. Khademinia, M. Dolatyari, A. Bakhtiari, H. Moradi, S. Saeidi, Int. Nano Lett. 3, 1 (2013).
50. F. M. Moghaddam and H. Saeidian, Mater. Sci. and Eng. B 139, 265 (2007).
51. Y. Chen, R. Yu, Q. Shi, J. Qin, F. Zheng, Mater. Lett. 61, 4438 (2007).
52. T. Tsuzuki and P. G. McCormick, Scripta Mater. 44, 1731 (2001).
53. M. R. Vaezi and S. K. Sadrnezhaad, Mater. Des. 28, 515 (2007).
54. M. Gusatti, J. A. Rosário, C. E. M. Campos, N. C. Kuhnen, E. U. Carvalho, H. G. Riella and A. M. Bernardin, J. Nanosci. Nanotechnol. 10, 4348 (2010).
55. M. Gusatti, C. E. M. Campos, J. A. Rosário, D. A. R. Souza, N. C. Kuhnen, H. G. Riella, J. Nanosci. Nanotechnol. 11, 5187 (2011).
56. M. Kang, S.-Y. Lee, C.-H. Chung, S. M. Cho, G. Y. Han, B.-W. Kim, K. J. Yoon, J. Photochem. Photobiol. A: Chem. 144, 185 (2001).
57. X. Wu, Q. Z. Jiang,Z. F. Ma, M. Fu, W. F. Shangguan, Solid State Commun. 136, 513 (2005).
58. J. Yang, S. Mei, J. M. F. Ferreira, Mater. Sci. Eng. C 15, 183 (2001).
59. J. C. Colmenares, M. A. Aramendia, A. Marinas, J. M. Marinas, F. J. Urbano, Appl. Catal. A 306, 120 (2006).
60. M. A. Barakat, H. Schaeffer, G. Hayes, S. Ismat-Shah, Appl. Catal. B 57, 23 (2005).
61. X. Chen and S. S. Mao, Chem. Rev. 107, 2891 (2007).
62. C. C. Wang, Z. Zhang, J. Y. Ying, Nano Structured Mater. 9, 583 (1997).
63. Y. Li, T. J. White, S. H. Lim, J. Solid State Chem. 177, 1372 (2004).
64. L. Zhang, Y. Sun, H. Jiu, Y. Wang, Y. Fu, J. Zhang, Micro Nano Lett. 6, 927 (2011).
65. G. Liu, S. Zhang, X. Dong, J. Wang, Hindawi Publishing Corporation, J. Nanomater. 2010, 1 (2010).
66. M. Ahrén, L. Selegard, F. Soderlind, M. Linares, J. Kauczor, P. Norman, P.-O. Kall, K. Uvdal, J. Nanopart. Res. 14, 1006 (2012).
67. P. Tartaj, M. P. Morales, S. Veintemillas-Verdaguer, T. González-Carreno, C. J. Serna, J. Phys. D: Appl. Phys. 36, R182 (2003).
68. C. Feldmann, Solid State Sci. 7, 868 (2005).
69. M. A. Flores-González, M. Villanueva-Ibáñez, J. L. D. L. Santiago, E. P. Beas, O. Tillement, Superficies y Vacío 19, 23 (2006).
70. S. E. Shaheen, D. S. Ginley, G. E. Jabbour, MRS Bull. 30,10 (2005).
71. J. W. Rasmussen, E. Martinez, P. Louka, D. G. Wingett, Expert Opin Drug Deliv. 7, 1063 (2010).
72. B. Liu and H. C. Zeng, J. Phys. Chem. B 108, 5867 (2004).
73. X. Y. Zhang, J. Y. Dai, H. C. Ong, N. Wang, H. L. W. Chan, C. L. Choy, Chem. Phys. Lett. 393, 17 (2004).
74. M. Gusatti, J. A. Rosário, G. S. Barroso, C. E. M. Campos, H. G. Riella, N. C. Kuhnen, Chemical Engineering Transactions 17, 1017 (2009).
75. M. R. Vaezi, J. Mater. Process. Technol. 205, 332 (2008).
76. M. Gusatti, C. E. M. Campos, D. A. R. Souza, N. C. Kuhnen, H. G. Riella, P. S. Pizani, J. Nanosci. Nanotechnol. 12, 7986 (2012).
77. M. Gusatti, D. A. R. Souza, V. M. Moser, N. C. Kuhnen, H. G. Riella, J. Nanoeng. Nanomanuf. 3, 15 (2013).

78. M. Gusatti, C. E. M. Campos, D. A. R. Souza, V. M. Moser, N. C. Kuhnen, H. G. Riella, J. Nanosci. Nanotechnol. 13, 8307 (2013).
79. Q. Ahsanulhaq, S. H. Kim, J. H. Kim, Y. B. Hahn, Mater. Res. Bull. 43, 3483 (2008).
80. R. Wahab, I. H. Hwang, Y.-S. Kim, H.-S. Shin, Chem. Eng. J. 168, 359 (2011).
81. R. Wahab, S. G. Ansari, Y. S. Kim, H. K. Seo, G. S. Kim, G. Khang, H.-S. Shin, Mater. Res. Bull. 42, 1640 (2007).
82. Inorganic Crystal Structure Database (ICSD), Gmelin-Institut für Anorganische Chemie and Fachinformationszentrum, FIZ, Karlsruhe, (2007).
83. D. Polsongkram, P. Chamninok, S. Pukird, L. Chow, O. Lupan, G. Chai, H. Khallaf, S. Park, A. Schulte, Physica B 403, 3713 (2008).
84. H. Zhang, D. Yang, Y. Ji, X. Ma, J. Xu, D. Que, J. Phys. Chem. B 108, 3955 (2004).
85. N. Uekawa, R. Yamashita, Y. J. Wu, K. Kakegawa, Phys. Chem. Chem. Phys. 6, 442 (2004).
86. E. V. Shevchenko, D. V. Talapin, H. Schnablegger, A. Kornowski, Ö. Festin, P. Svedlindh, M. Haase, H. Weller, J. Am. Chem. Soc. 125, 9090 (2003).
87. W.-J. Li, E.-W. Shi, Y.-Q. Zheng, Z.-W. Yin, J. Mater. Sci. Lett. 20, 1381 (2001).
88. L. Wang and M. Muhammed, J. Mater. Chem. 9, 2871 (1999).
89. S. Sepulveda-Guzman, B. Reeja-Jayan, E. Rosa, A. Torres-Castro, V. Gonzalez-Gonzalez, M. Jose-Yacaman, Mater. Chem. Phys. 115, 172 (2009).
90. Z. Wang, X.-F. Qian, J. Yin, Z.-K. Zhu, Langmuir 20, 3441 (2004).
91. A. Umar, S. H. Kim, J. H. Kim, A. Al-Hajry, Y. B. Hahn, J. Alloys Compd. 463, 516 (2008).
92. Y. Sheng, Y. Jiang, X. Lan, C. Wang, S. Li, X. Liu, H. Zhong, J. Nanomater. 2011, 473629-1 (2011).
93. H. Zhang, D. Yang, X. Ma, Y. Ji, J. Xu, D. Que, Nanotechnology 15, 622 (2004).
94. Z. Hu, G. Oskam, R. L. Penn, N. Pesika, P. C. Searson, J. Phys. Chem. B 107, 3124 (2003).
95. G. P. Barreto, G. Morales, M. L. L. Quintanilla, J. Mater. 2013, 11 (2013).
96. L. Xu, Y. Guo, Q. Liao, J. Zhang, D. Xu, J. Phys. Chem. B 109, 13519 (2005).
97. Y. Sun, D. J. Riley, M. N. R. Ashfold, J. Phys. Chem. B 110, 15186 (2006).
98. S. Rani, P. Suri, P. K. Shishodia, R. M. Mehra, Sol. Energ. Mat. Sol. C 92, 1639 (2008).
99. P. Li, H. Liu, Y.-F. Zhang, Y. Wei, X.-K. Wang, Mater. Chem. Phys. 106, 63 (2007).
100. X. Shen, Y. Zhai, Z. Ning, J. Mater. Sci. Technol. 29, 44 (2013).
101. J. H. Yang, J. H. Zheng, H. J. Zhai, L. L. Yang, L. Liu, and M. Gao, Cryst. Res. Technol. 44, 619 (2009).
102. A. Wei, X. W. Sun, C. X. Xu, Z. L. Dong, Y. Yang, S. T. Tan, W. Huang, Nanotechnology 17, 1740 (2006).
103. N. R. N. Roselina and A. Azizan, Procedia Engineering 41, 1620 (2012).
104. L. K. Kurihara, G. M. Chow, P. E. Schoen, Nanostruct. Mater. 5, 607 (2008).
105. N. R. N. Roselina, A. Azizan, Z. Locman, Sains Malays. 41, 1037 (2012).
106. C. Feldmann, H. O. Jungk, Angew. Chem. 113, 372 (2001).
107. C. Feldmann, Adv. Funct. Mater. 13, 101 (2003).
108. C. J. Belle and U. Simon, Combinatorial approaches for synthesis of metal oxides: processing and sensing application, In: M. A. Carpenter, S. Mathur, A. Kolmakov (ed.), Metal Oxide Nanomaterials for Chemical Sensors, Springer, New York, p. 117-166, (2013).
109. F. Fiévet and R. Brayner, The polyol process, In: R. Brayner, F. Fiévet, T. Coradin (ed.), Nanomaterials: A Danger or a Promise? - A Chemical and Biological Perspective, Springer, London, p. 1-26, (2013).
110. G. G. Couto, J. J. Klein, W. H. Schreiner, D. H. Mosca, A. J. A. Oliveira, A. J. G. Zarbin, J. Colloid Interface Sci. 311, 461 (2007).

111. T. Dey, Magnetic nanoparticles and cellulosic nanofibers to remove arsenic and other heavy metals from water, In: T. Dey (ed.), Nanotechnology for Water Purification, Universal-Publishers, Florida, p. 1-28, (2012).
112. P. Toneguzzo, G. Viau, O. Acher, F. Guillet, E. Bruneton, F. Fievet, J. Mater. Sci. 35, 3767 (2000).
113. Y. Tian, J.H. Fendler, Chem. Mater. 8, 468 (1996).
114. D. Mott, J. Galkowski, L. Wang, J. Luo, C. J. Zhong, Langmuir 23, 5740 (2007).
115. Y. Chen, K. Y. Liew, J. Li, Mater. Lett. 62, 1018 (2007).
116. U. Koch, A. Fojtik, H. Weller, A. Henglen, Chem. Phys. Lett. 122, 507 (1985).
117. C. Feldmann, Scripta Mater. 44, 2193 (2001).
118. J. Merikhi, H.-O. Jungk, C. Feldmann, J. Mater. Chem. 10, 1311 (2000).
119. R. Bazzi, M.A. Flores-Gonzalez, C. Louis, K. Lebbou, C. Dujardin, A. Brenier, W. Zhang, O. Tillement, E. Bernstein, P. Perriat, J. Lumin. 102/103, 445 (2003).
120. R. Bazzi, A. Brenier, P. Perriat, O. Tillement, J. Lumin. 113, 161 (2005).
121. B. D. Cullity and S. R. Stock, Elements of X-ray Diffraction, Prentice Hall, New Jersey, (2001).
122. N. Goswami and D. K. Sharma, Physica E 42, 1675 (2010).
123. F. Soderlind, H. Pedersen, R. M. J. Petoral, P.-O. Kall, K. Uvdal, J. Colloid Interface Sci. 288, 140 (2005).
124. M.-A. Fortin, R. M. J. Petoral, F. Soderlind, A. Klasson, M. Engstrom, T. Veres, P.-O. Kall, K. Uvdal, Nanotechnology 18, 395501 (2007).
125. L. Faucher, A.-A. Guay-Begin, J. Lagueux, M.-F. Cote, E. Petitclerc, M.-A. Fortin, Contrast Media Mol. Imag. 6, 209 (2011).
126. C. J. Brinker and G. W. Scherer, Sol-Gel Science: The physics and chemistry of sol-gel processing, Academic Press Inc., London, (1990).
127. C. Su, B. Y. Hong, C. M. Tseng, Catal. Today 96, 119 (2004).
128. J. A. Chang, M. Vithal, I. C. Baek, S. I. Seok, J. Solid State Chem. 182, 749 (2009).
129. J. N. Lalena, D. A. Cleary, E. E. Carpenter, N. F. Dean, Inorganic materials synthesis and fabrication, John Wiley & Sons Inc., New Jersey, (2008).
130. J. D. Mackenzie and E. P. Bescher, Acc. Chem. Res. 40, 810 (2007).
131. H. Mehranpour, M. Askari, M. S. Ghamsari, Nucleation and Growth of TiO_2 Nanoparticles, In: M. M. Rahman (ed.), Nanomaterials, Intech, Croatia, p. 3-26, (2011).
132. O. Carp, C. L. Huisman, A. Reller, Prog. Solid State Ch. 32, 33 (2004).
133. A. Kumar, Gaurav, A. K. Malik, D. K. Tewary, B. Singh, Anal. Chim. Acta 610, 1 (2008).
134. A. C. Pierre, Introduction to Sol-Gel Processing, Klumer Academic Publisher, Boston, (1998).
135. F. Rataboul, C. Nayral, M.-J. Casanove, A. Maisonnat, B. Chaudret, J. Organomet. Chem. 643-644, 307 (2002).
136. M. Niederberger and N. Pinna, Metal Oxide Nanoparticles in Organic Solvents: Synthesis, Formation, Assembly and Application, Springer Dordrecht Heidelberg, New York, (2009).
137. D. C. Bradley, R. C. Mehrotra, I. P. Rothwell, A. Singh, Alkoxo and aryloxo derivatives of metals, Academic Press, London, (2001).
138. N. Y.Turova, E. P. Turevskaya, V. G. Kessler, M. I. Yanovskaya, The chemistry of metal alkoxides, Kluwer Academic Publishers, Boston, (2002).
139. S. Sakka (ed.), Handbook of sol-gel science and technology: processing, characterization and applications, Kluwer Academic Publishers, New York, (2004).
140. J. T. Davies and E. K. Rideal, Interfacial phenomena, Academic Press, New York, (1963).

141. G. Cao and Y. Wang, Nanostructures and Nanomaterials: Synthesis, Properties, and Applications, World Scientific Series, Singapore, (2011).

142. W. Zhou, Q. Cao, S. Tang, Powder Technol. 168, 32 (2006).

143. E. H. Lan and B. Dunn, Processing and applications of sol-gel glass, In: N. P. Bansal and A. R. Boccaccini (ed.), Ceramics and Composites Processing Methods, John Wiley e Sons Inc., New Jersey, p. 183-198, (2012).

144. L. L. Hench and J. K. West, Chem. Rev. 90, 33 (1990).

145. B. Li and W.-H. Zhong, Liquid-Phase synthesis, In: W.-H. Zhong, B. Li, R. G. Maguire, V. G. Dang, J. A. Shatkin, G. M. Gross, M. C. Richey (ed.), Nanoscience and Nanomaterials: Synthesis, Manufacturing and Industry Impacts, Destech Publications Inc., Pennsylvania, p.57-98, (2012).

146. M. V. Landau, Sol-gel process, In: G. Ertl, H. Knözinge, F. Schüth, J. Weitkamp (ed.), Handbook of heterogeneous catalysis, John Wiley and Sons, p. 119-160, (1999).

147. B. Dunn and J. I. Zink, Acc. Chem. Res. 40, 747 (2007).

148. J. D. Wright and N. A. J. M. Sommerdijk, Sol-gel materials: chemistry and applications, CRC Press, Florida, (2000).

149. S. W. Boettcher, J. Fan, C.-K. Tsung, Q. Shi, G. D. Stucky, Acc. Chem. Res. 40, 784 (2007).

150. A. Fidalgo, M. E. Rosa, L. M. Ilharco, Chem. Mater. 15, 2186 (2003).

151. R. Ciriminna, A. Fidalgo, V. Pandarus, F. Béland, L. M. Ilharco, M. Pagliaro, Chem. Rev. 113, 6592 (2013).

152. J. Zhang, Q. Xu, M. Li, Z. Feng, C. Li, J. Phys. Chem. C 113, 1698 (2009).

153. H. A. D`Alesio, Synthesis of nanostructured titaniun oxide, Thesis, Federal University of Santa Catarina, Chemical Engineering Department, Brazil, p. 1-87, (2013).

154. E. A. Barringer and H. K. Bowen, Langmuir 1, 414 (1985).

155. M. Gotić, M. Ivanda, A. Sekulić, S. Musić, S. Popović, A. Turković, K. Furić, Mater. Lett. 28, 225 (1996).

156. N.-L. Wu, Bull. Coll. Eng., N.T.U. 84, 85 (2002).

157. M. Addamo, M. Bellardita, A. Di Paola, L. Palmisano, Chem. Commun. 4943 (2006).

158. A. C. Larson and R. B. Von Dreele, General Structure Analysis System (GSAS), Los Alamos National Laboratory Report LAUR 86-748, (2000).

159. B.H. Toby, J. Appl. Cryst. 34, 210 (2001).